Nano Research 2014, 7(11): 1670–1679
DOI 10.1007/s12274-014-0527-7
Research Article
ISSN 1998-0124
CN 11-5974/O4

Solvent switching and purification of colloidal nanoparticles through water/oil Interfaces within a density gradient

Yun Kuang, Sha Song, Xiaofei Liu, Minglin Li, Zhao Cai, Liang Luo, and Xiaoming Sun (✉)

State Key Laboratory of Chemical Resource Engineering, Beijing University of Chemical Technology, Beijing 100029, China

Received: 12 May 2014
Revised: 26 June 2014
Accepted: 27 June 2014

KEYWORDS
density gradient, water/oil interface, solvent switching, purification

ABSTRACT

Traditional post-treatment of colloidal nanoparticles (NPs) usually involves repeated centrifugation–wash–sonication processes to separate NPs from the original synthetic environment; however, such separation processes have either high energy cost or low efficiency and tend to cause aggregation. Here we show a general and scalable colloid post-processing technique based on density gradient centrifugation through water/oil interfaces. Such a one-step technique can switch the solvent in a colloid at almost any concentration without aggregation, and meanwhile purify colloidal nanoparticles by separating them from by-products and environmental impurities. Droplet sedimentation was shown to be the mechanism of this one-step concentration/purification process, and mathematical modeling was established to quantify the accumulation and sedimentation velocities of different NPs.

Colloidal nanoparticles (NPs) with tunable size, shape, and surface functional groups [1–3] have wide applications in catalysis [4–6], energy conversion [7–9], and bio-related areas [10–12]. They can also act as building blocks for complex highly ordered nanodevices [13–15]. In practice, any of the above applications requires "pure", "clean" colloidal NPs suspended in the "right" medium. Here "pure" refers to monodisperse, "clean" means no other additives are used in purification of NPs and the "right" medium is a key factor for specific applications. Traditional post-treatment of colloidal NPs usually uses repeated centrifugation–wash–sonication processes to separate NPs from the original synthetic environment [16]; however, such separation processes have either high energy cost or low efficiency, and tend to cause significant loss of NPs in the supernatant, especially for small NPs. Besides, repeated wash–sonication will lead to irreversible aggregation of colloidal NPs because of the detachment of coating surfactant or ligands that are needed to stabilize the NPs [17]. Therefore, developing a simple, versatile, low-cost and efficient post-processing technique is a big challenge with urgent priority.

Address correspondence to sunxm@mail.buct.edu.cn

Herein, we report a universal and scalable colloid processing technique based on density gradient centrifugation [18–24] through water/oil (W/O) interfaces. The technique is applicable for colloidal nanoparticles suspended in either aqueous or organic solvents. Such a one-step post-processing technique can selectively switch colloids to a desired solvent at almost any concentration without aggregation, even when approaching the concentration limit where particles are closely packed. Meanwhile, when the nanoparticles were forced to pass through a solvent in which they are insoluble, only a small fraction ($<10^{-4}$) of the original solvent was brought down while > 99.9% of the particles were purified. Furthermore, the switching process has some selectivity for nanoparticles with different size or morphologies. All these features made such a post-processing technique an efficient tool for practical purification of NPs.

Figures 1(a) and 1(c) schematically show solvent switching and concentration control of both aqueous and organic soluble colloidal NPs through a three layer density gradient with layers in which the NPs were soluble on the top and bottom and a layer in which they were insoluble in the middle. That is, the original colloids were laid on a layer in which the NPs were insoluble while the target solvent was placed at the bottom. Before centrifugation, large interfacial tension and media density differences stabilized the interfaces and made the three layers stable and separate. When a centrifugal field was applied, NPs were forced to pass through the layer in which they were insoluble and then became dissolved in a new solvent.

The solvent switching concept was demonstrated using NPs soluble in aqueous and organic solvents as examples (Figs. 1(b) and 1(d)). Details of the syntheses of the NPs are given in the Electronic Supplementary Material (ESM). For example, after centrifugation, polyvinylpyrrolidone (PVP) coated PtCu alloy nanoparticles could be transferred from ethanol into water, ethylene glycol (EG), N,N-dimethylmethanamide (DMF), acetone, acetonitrile, tetrahydrofuran (THF) and pyridine by passing through an insoluble layer composed of 5% CCl_4 solution in cyclohexane (Fig. 1(B)). However, since acetone and acetonitrile have lower

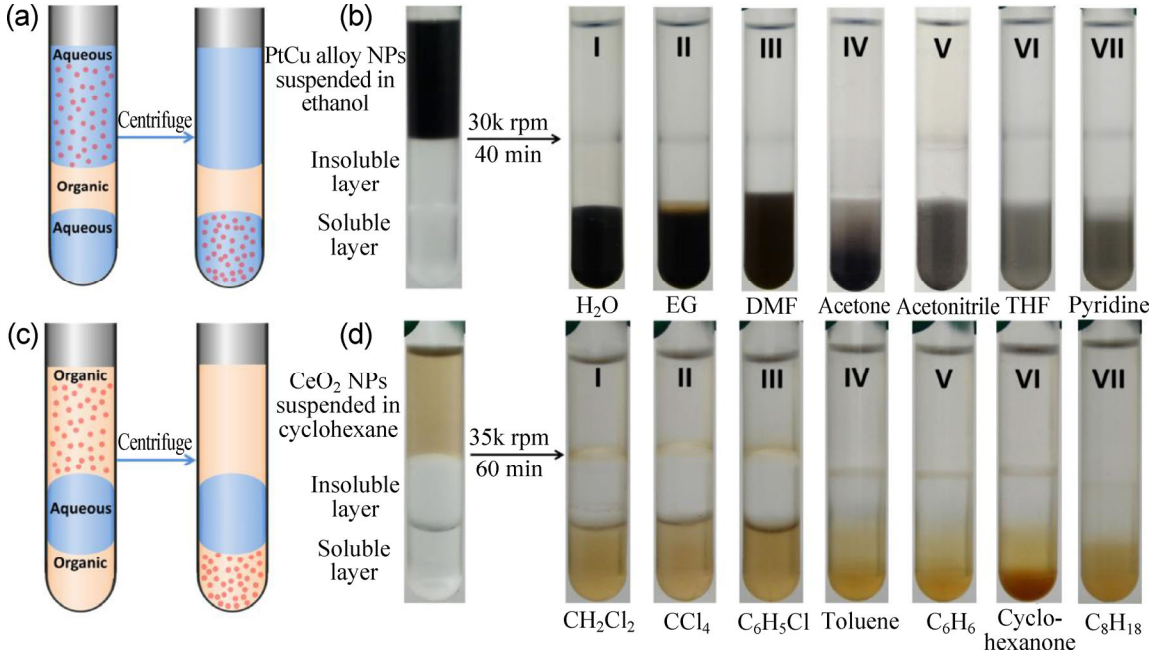

Figure 1 Schematic of solvent switching and concentration control of both (a) aqueous and (c) organic soluble colloidal NPs through water/oil interfaces. (b) Solvent switching of PtCu alloy NPs from ethanol to (I) water, (II) EG, (III) DMF, (IV) acetone, (V) acetonitrile, (VI) THF and (VII) pyridine. (d) Solvents switching of CeO_2 NPs from cyclohexane to (I) methylene chloride, (II) carbon tetrachloride, (III) chlorobenzene, (IV) toluene, (V) benzene, (VI) cyclohexanone and (VII) octane.

densities than 5% CCl_4/cyclohexane solution, mixed solvents containing 30% of water in volume were used. The range of possible soluble layers demonstrates the versatility of this post-processing technique. However, the as purified colloids showed different colour depth because of solubility differences. Similarly, oleic acid coated CeO_2 NPs suspended in cyclohexane were transferred into methylene chloride, carbon tetrachloride, chlorobenzene, cyclohexanone, octane, toluene and benzene through a water layer (Fig. 1(d)). Since some of the organic solvents have lower densities than water, a low density solvent, ethanol, was used as the insoluble layer when making the density gradients. Because these organic solvents are miscible with ethanol in a certain ratio, the interfaces were unclear, as shown in Fig. 1(dIV)–(dVII).

Besides solvent diversity, such a one-step post-processing method is also independent of the morphologies of the nanoparticles. Figure 2 shows solvent switching of Au nanoparticles (Fig. 2(a)), nanorods (Fig. 2(b)) and layered double hydroxide nanosheets (Fig. 2(c)) from water to 50% ethylene glycol solution by passing through a 30% CCl_4/cyclohexane layer. It should be noted that 50% ethylene glycol solution causes great aggregation of hexadecyltrimethylammonium chloride (CTAC) coated Au nanoparticles because CTAC has a much higher solubility in ethylene glycol than in water, and thus 1 mM of CTAC was added into the aqueous layer to avoid aggregation of Au nanostructures. TEM images and UV–Vis spectra clearly showed that the as purified Au nanoparticles and nanorods did not aggregate.

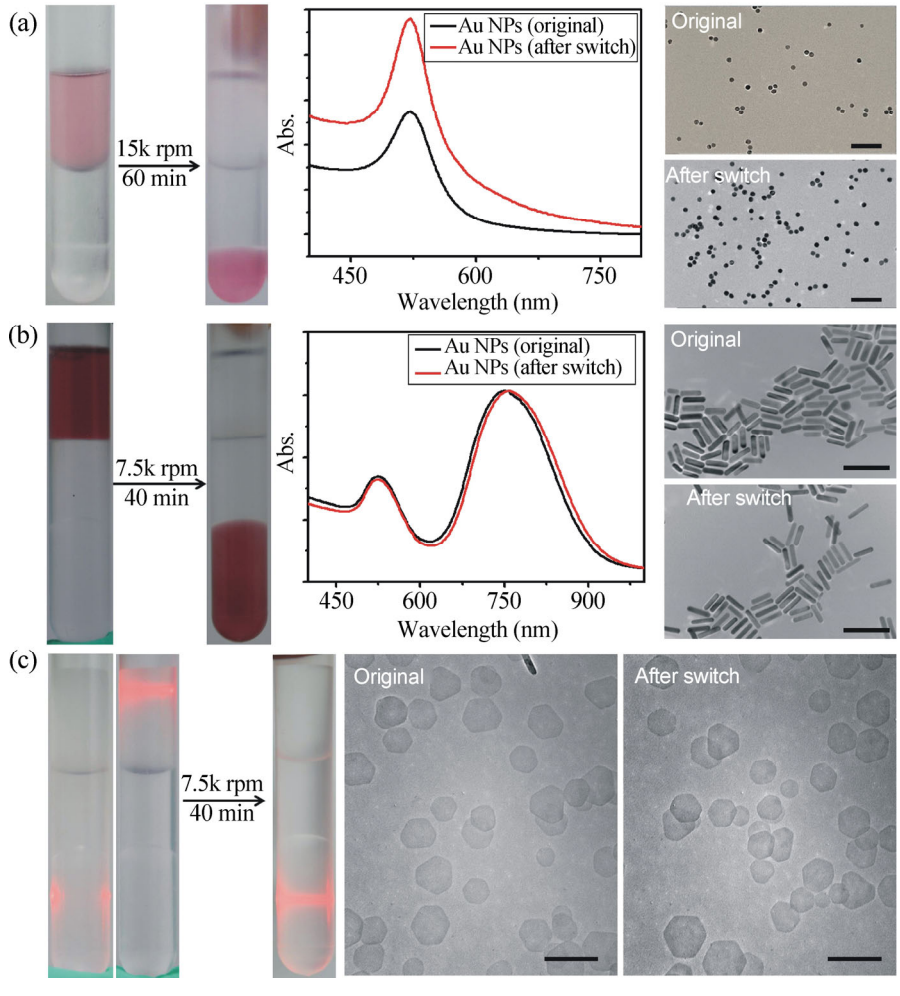

Figure 2 (a) Digital camera images, UV–Vis spectra and TEM images of Au nanoparticles. (b) Digital camera images and UV–Vis spectra of Au nanorods. (c) Digital camera and TEM images of layered double hydroxides before and after solvent switch. Scale bars are 100 nm in (a), (b) and 200 nm in (c).

Tyndall effects (using a red laser) and TEM images also confirmed that layered double hydroxide nanosheets were in a colloidal state. However, as this method is based on density gradient and interfacial blocking, some nanosheets with very low density—such as graphene oxide nanosheets—could not pass through the interface (Fig. S1 in the ESM).

By altering the volume ratio between upper and bottom layers, different concentrations could be obtained. As shown in Fig. 3, Au nanoparticle solutions with different volumes were suspended on top of a three layer gradient. After centrifugation, NPs were totally switched from the upper solution to the bottom solvent. When the volume ratio between the upper layer and bottom layer increased, the concentration increased, as demonstrated by the increasing intensities of absorbance (Figs. 3(b) and 3(c)). A linear relationship between concentration and volume ratio was also observed (Fig. 3(d)), leading us to find the concentration limit.

To verify how much solvent was carried into the bottom layer, the volume of the bottom layer was minimized to zero. Then a two-layer gradient was made with aqueous Au nanoparticle solution on the top and 30% CCl_4/C_6H_{12} solution at the bottom (Fig. 4(a)).

After centrifugation, nearly all of the Au NPs passed the interface and sedimented at the bottom of the tube. Since the volume is too small to measure directly, we used an indirect linear curve fitting method to calculate it. We used spectroscopy to detect the concentration of the Au nanoparticle solution. We assume that the concentration and volume of the nanoparticle solution brought down by centrifugation was C_0 and V_0, respectively. After adding a volume of water V_n to the ultraconcentrated solution, the concentration of nanoparticle solution became C_n. In contrast to the C_0 value (too high) and the V_0 value (too small), V_n can be directly measured by pipet and C_n could be calculated using UV–Vis spectroscopy based on the Beer–Lambert law (see Fig. 4(c) for details of the dilution procedure). Since the total amount of Au nanoparticles was kept the same, Eq. (1) could be established, as shown below

$$C_n(V_n + V_0) = C_0V_0 \quad (1)$$

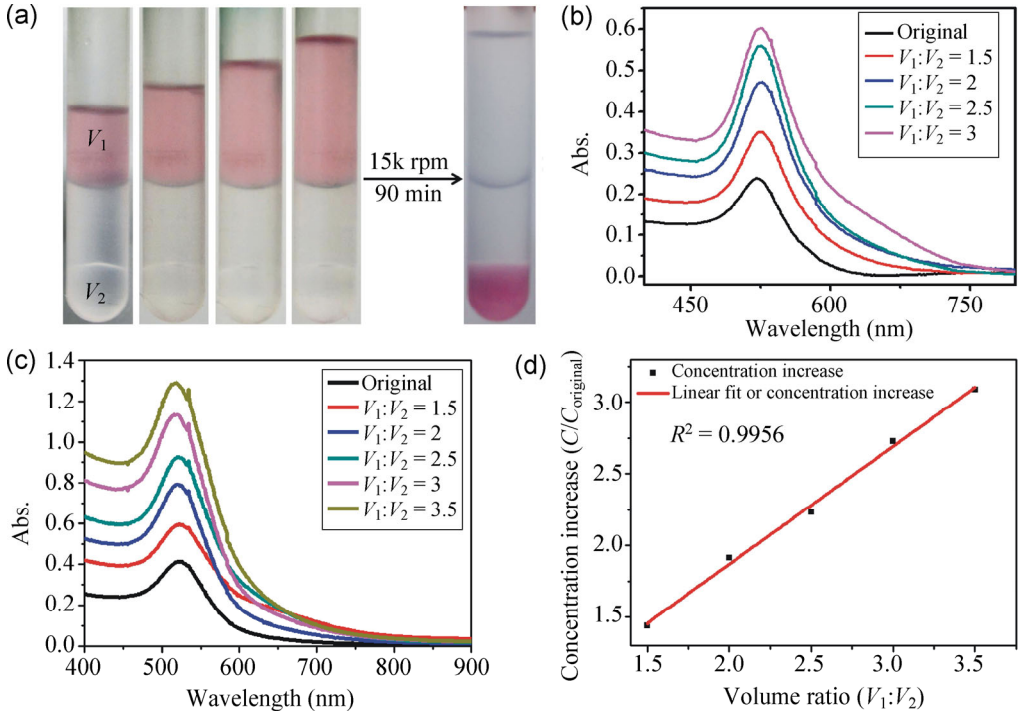

Figure 3 (a) Digital camera images and (b) UV–Vis spectra of aqueous Au solutions before and after solvent switching. (c) UV–Vis spectra of Au nanoparticles switched from cyclohexane to 30% CCl_4/cyclohexane with different volume ratios. (d) Linear fitting of concentration increase vs. volume ratio.

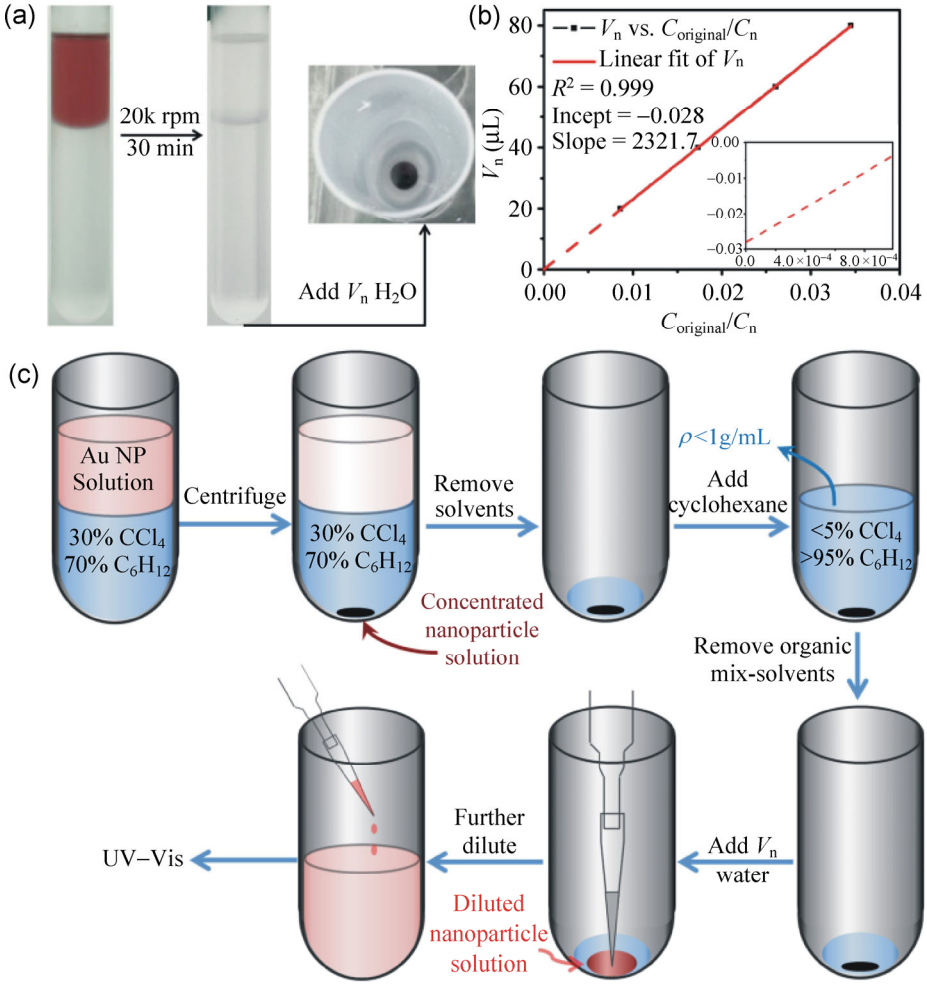

Figure 4 (a) Digital camera images of aqueous Au solutions before and after concentration. (b) Linear fitting of V_n vs. $C_{original}/C_n$ to calculate the concentration increase and total volume brought down. (c) Schematic illustration of dilution and liquid seal of the as concentrated nanoparticle solution after centrifugation.

It should be noted that the liquid seal afforded by the insoluble solvent is important to ensure accurate measurement of the amount of water in the nanoparticle solutions at the bottom of the tubes after centrifugation. By introducing $C_{original}$ to make calculation based on all measurable parameters, Eq. (1) can be transformed into

$$V_n = C_0V_0/C_n - V_0 = (C_0/C_{original})V_0/(C_n/C_{original}) - V_0 \quad (2)$$

where $C_{original}$ equals the concentration of the original Au nanoparticle solution before centrifugation. By plotting V_n versus $C_{original}/C_n$, a linear plot with intercept equal to $-V_0$ and slope equal $(C_0/C_{original})V_0$ can be drawn, and then as the total volume V_0 and concentration increase, $C_0/C_{original}$ of the as concentrated nanoparticle solution could be obtained. In this case, 3 mL of original Au nanoparticle solution was concentrated to no more than 0.1 μL (average results of three tests: 0.028 μL) after centrifugation and the concentration increased at least 10^4 times (see the inset of Fig. 4(b)). The as concentrated nanoparticle solutions even exhibited a solid state at the bottom of the tubes. At such extremely high concentration, the density of the nanoparticle solution was estimated to be 5.28 g/mL and the packing density of nanoparticles was 64.2%, which is close to the concentration limit where particles are closely packed (5.93 g/mL, packing density 74%), demonstrating the wide concentration tuning range afforded by this solvent switching technique.

In addition, the solvent switching technique is an efficient purification tool to remove environmental

impurities. As mentioned above, 3 mL of Au nanoparticle solution was concentrated to less than 0.03 μL. When the as concentrated nanoparticle solution was diluted to the original volume with a pure solvent, only a small proportion (10^{-4}) of impurities remained. At the same time, the switching efficiency was quite high for nanoparticles, with more than 99.9% of nanoparticles transferred to the bottom solvent after the switching procedure (Fig. S2, in the ESM).

Removal of environmental impurities could reach very low ligand content in the solution, which sometimes leads to partial aggregation of nanoparticles when a weakly adsorbed ligand was used to stabilize the nanoparticles. For example, Au nanoparticles stabilized by the weak ligand trisodium citrate (TSC) aggregated seriously after solvent switching because of dissociation of their surface ligands in the clean solvent. However, nanoparticles coated with the strongly adsorbed surface ligand PVP did not aggregate due to the well stabilized surface. When the moderately well adsorbed ligand CTAC was used to stabilize Au nanoparticles, the extent of aggregation depends on particle size—only nanoparticles larger than 50 nm became aggregated. This might because there was insufficient CTAC brought down to stabilize the nanoparticle surfaces. Therefore, when we only want to remove by-products rather than ligands, a small amount of surface ligands should be added to the bottom solution to avoid aggregation in the case of weakly bound ligands.

The solvent switching method is also an efficient separation tool. Figure 5 shows the separation of different sized Au nanoparticles in a three layer density gradient. TEM images (Figs. 5(c) and 5(d)) show that 20 and 50 nm sized AuNPs are separated, as confirmed by their UV–Vis spectra, with the surface plasmon resonance peak of 20 and 50 nm sized Au NPs located at 521 and 528 nm, respectively. However, compared with pure 20 and 50 nm nanoparticle solutions, the as separated solutions showed a slight red shift, possibly because some small by-products existed in the original 50 nm NP solution and stayed

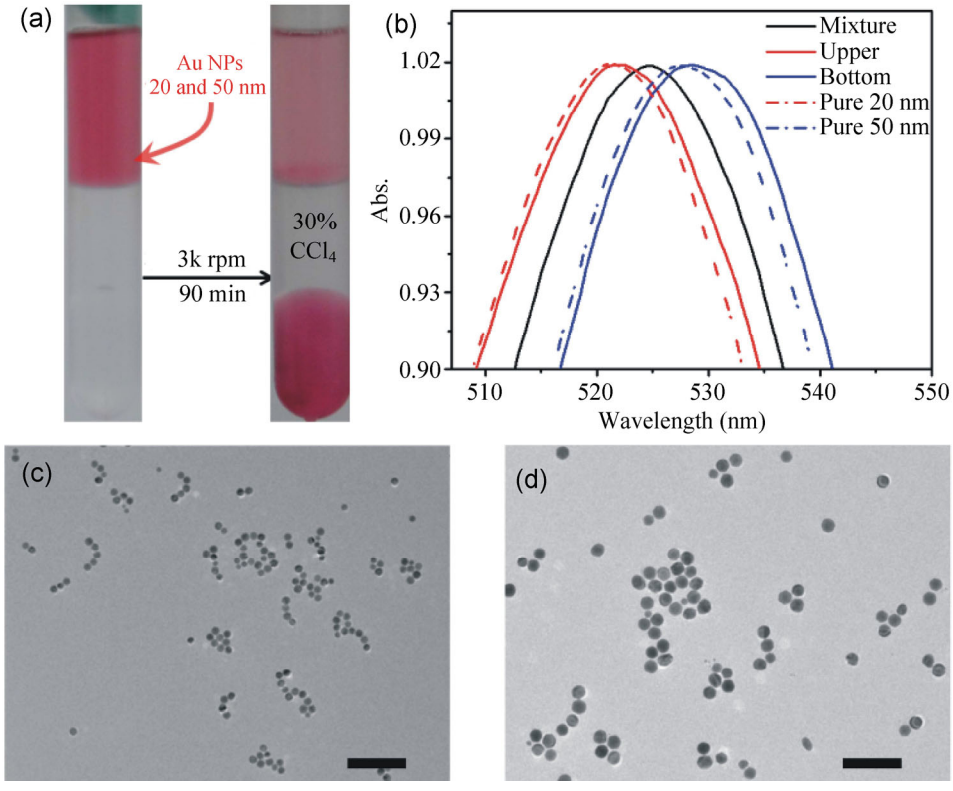

Figure 5 (a) Digital camera images of mixed Au nanoparticle solution (20 and 50 nm NPs) before and after solvent switching. (b) UV–Vis spectra of the mixture, the upper and bottom solutions after separation, and pure 20 and 50 nm nanoparticle solutions. TEM images of (c) upper solution and (d) bottom solution after separation. Scale bars are 200 nm.

in the upper layer after separation.

Interestingly, the interface separation method is also applicable to nanoparticles with the same composition, volume and mass, but different morphologies. As a typical example, Fig. 6 shows the separation of Au nanoparticles (20 nm in diameter, 4,185 nm^3 in volume) and nanorods (NRs) (9.8 nm in diameter, 58 nm in length, 4,372 nm^3 in volume). UV–Vis spectra clearly reveal that the nanoparticles and nanorods were separated—which is quite hard to achieve using other separation means—although the separation was not complete.

In order to reveal why nanoparticles with different size and norphologies could be separated and why they have different sedimentation behaviour, the time dependent sedimentation process was monitored. Figure 7 plots sedimentation percentages of 20, 50 nm nanoparticles and nanorods at different time points. The curves show totally different sedimentation behaviors for the three types of NPs: 50 nm nanoparticles passed through the interface much faster than 20 nm nanoparticles, especially under low centrifugal force (<5k rpm, about 4,286g), while the sedimentation behavior of 20 nm nanoparticles and nanorods showed a definite difference only under a suitable centrifugal force range (4k–7k rpm, about 2,743g–8,402g). Lower centrifugal force could not make the NPs efficiently accumulate while higher centrifugal force led to fast sedimentation of all kinds of NPs. Both effects decreased the separation efficiency. Such differences in sedimentation behavior allowed the 20 nm nanoparticles to be well separated from the 50 nm nanoparticles at 3k rpm (Fig. 5) but only particially separated from nanorods at 7 k rpm (Fig. 6).

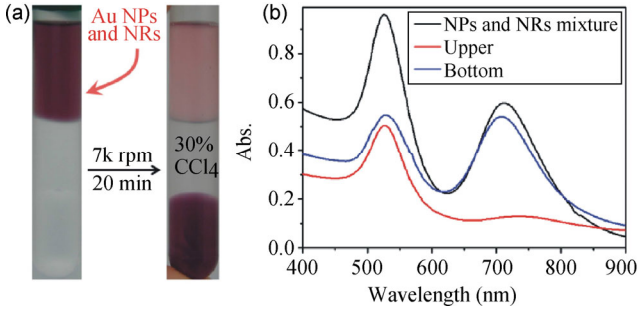

Figure 6 (a) Digital camera images of mixed Au nanoparticles (20 nm) and nanorods (average diameter: 9.8 nm, average length: 58 nm, see Fig. 2(b)) solution before and after solvent switching. (b) UV–Vis spectra of the mixture, and the upper and bottom solutions after separation.

Based on the analysis of the sedimentation curves, we propose that the solvent switching process involves two stages: Accumulation of NPs at the interface and droplet sedimentation through the interface [25] (Fig. 8), both of which are driven by centrifugal force.

Under low centrifugal force, the sedimentation curves show an obvious platform at the initial stage, which evidenced the accumulation process before sedimentation through the interface. Following the accumulation platform was a quick drop in NP percentage, demonstrating the passing of the NPs through the interface. Because NPs have large curvatures, they suffer large interfacial tension at the interface and get blocked. Therefore, NPs must group together to form larger droplets to break the interface and then pass through the insoluble layer. We call this process "droplet sedimentation" [25].

A mathematical model was established to demonstrate the droplet sedimentation mechanism. At the water/oil interface, nanoparticles/droplets suffer three forces (Fig. 8(a)): The centrifugal force F_c, the buoyancy F_b and the interfacial tension F_i, whose expressions are listed below

$$F_c = mg' = \frac{4}{3}\pi r^3 \rho_p g' \tag{3}$$

$$F_i = mg' = 2\gamma\pi r \sin^2\theta \tag{4}$$

$$F_b = \rho_w g' V_w + \rho_o g' V_o \approx \rho_w g' V_p = \frac{4}{3}\pi r^3 \rho_w g' \tag{5}$$

where m denotes the mass of the nanoparticles, g' denotes centrifugal acceleration, r denotes the diameter of the nanoparticle, ρ_p denotes the density of the nanoparticle, γ denotes the interfacial tension coefficient, θ denotes the contact angle between the nanoparticles and the interface, V_p denotes the volume of nanoparticles, and ρ_w and ρ_o denote the densities of the water layer and organic layer, respectively. Here ρ_w and ρ_o can be considered approximately equal since 30% CCl_4/C_6H_{12} has a density of 1.02 g/mL.

The critical condition for particles/droplets to pass through the interface is

$$F_c \geqslant F_b + F_i \tag{6}$$

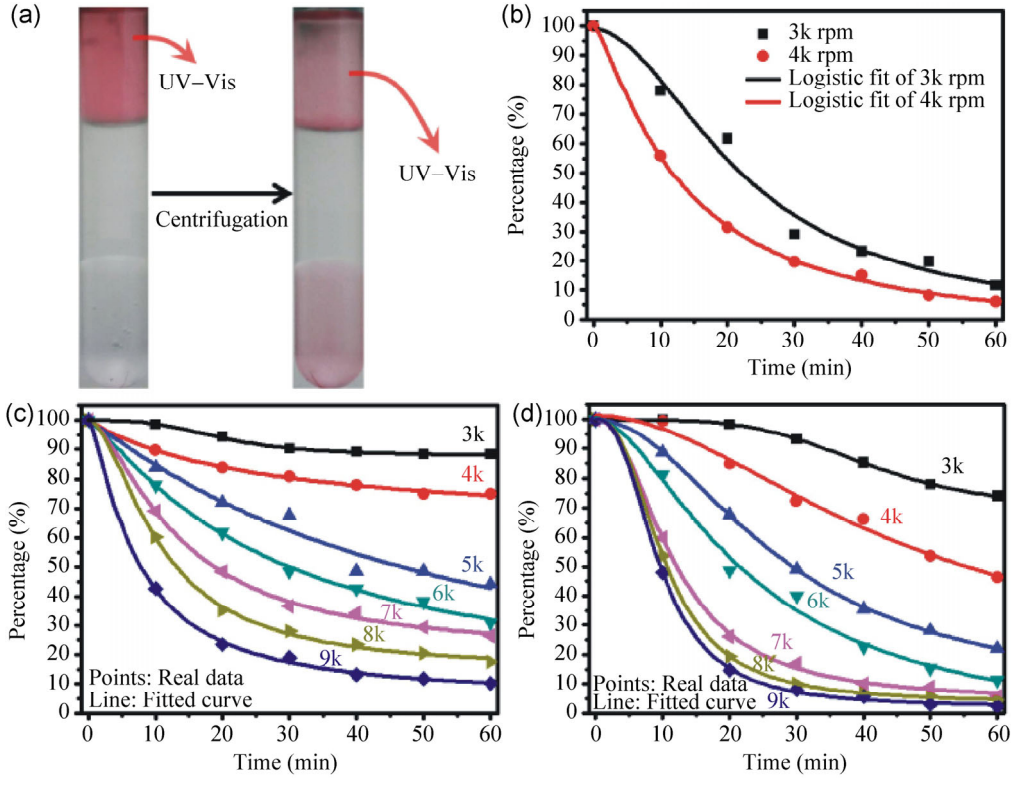

Figure 7 (a) Monitoring of time dependent sedimentation percentage based on the Beer–Lambert law and sedimentation curves of (b) 50 nm Au nanoparticles, (c) 20 nm Au nanoparticles and (d) Au nanorods. Points: Real data. Lines: Fitted curve based on the Logistic model.

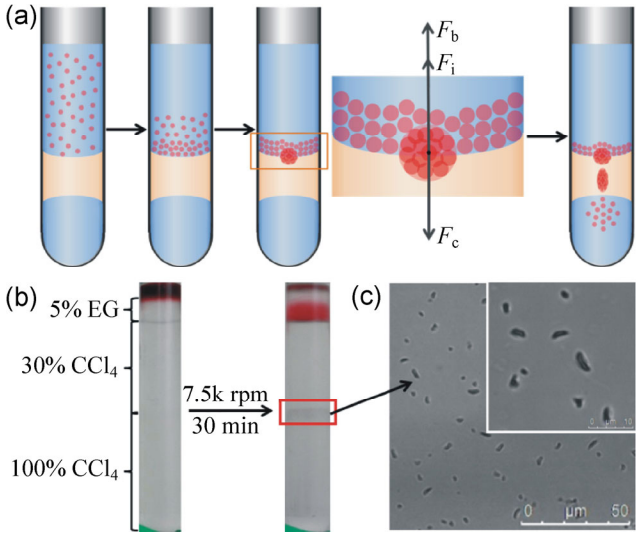

Figure 8 (a) Schematic illustration of droplet sedimentation; (b) capture of nanoparticle aggregated droplets through a four-layer density gradient; (c) microscopy images of the captured droplets.

Combining Eq. (3), (4), (5), (6) and considering that the nanoparticles have a t nm thick solvent layer coated on their surface and the droplet has a packing density of k, the critical condition for droplet sedimentation is calculated to be

$$\frac{kR^2}{(1+t/r)^3} \geqslant \frac{3\gamma}{2g'(\rho_c-\rho_w)} \quad (7)$$

where R denotes the diameter of the droplets and ρ_c denotes the density of the nanoparticle core.

We can conclude from Eq. (7): (1) Under certain centrifugal force, large nanoparticles have a low t/r value and thus accumulate into a small droplet which undergoes efficient sedimentation, while small nanoparticles (large t/r value) must accumulate into a large droplet before sedimentation. (2) For nanoparticles with given size, high centrifugal force leads to small droplets and faster sedimentation through the interface, which resulted in a faster percentage drop, while low centrifugal force causes large droplets and requires accumulation for a long time, which corresponds to the platforms in the sedimentation curves. We have also calculated the size of the droplets according to Eq. (7). For 20 nm CTAC coated Au nanoparticles, the size of the droplets was estimated to be at least 9.56 μm under 10,000g centrifugal force

(see the ESM for details of the calculations).

In order to experimentally verify the droplet sedimentation mechanism, we designed a four layer density gradient containing a buffer layer and two organic layers. A sharp CCl_4 concentration gradient was set (Fig. 8(b)) to capture the droplets. The buffer layer could exclude the influence of CTAC and self-aggregation of NPs at the interface. When a centrifugal field was applied, nanoparticles first sedimented into the buffer layer and then accumulated to form droplets at the W/O interface. When the droplets grew big enough, they passed through the insoluble layer. However, when the droplets fell on the interface between 30% and 100% CCl_4 layers, they could not move on because of the higher buoyancy arising from the higher density of the medium, and were thus blocked at this point. Since the droplets were very big, they could be observed under optical microscopy. As shown in Fig. 8(b), the captured droplets were 5–10 μm in size, which coincide with the calculation results, further confirming droplet sedimentation mechanism. When the centrifugal force was large enough, the platform before droplet sedimentation dispersed, resulting in faster accumulation and droplet sedimentation. However, new platforms formed after the rapid drop in concentration, and the platforms are correlated to the centrifugal force for colloids with a given nanoparticle size. This platform represents the critical concentration of NPs that can trigger droplet sedimentation. At this stage, a large concentration gradient between the upper solution and the interface led to fast diffusion of NPs from the accumulation to the solution and therefore resulted in an accumulation/diffusion equilibrium.

Based on this, a mathmatical model was established, which fitted very well with the Logistic model (Fig. 7, data points are real data and lines are fitted curves)

$$P = \frac{100 - P_0}{1 + (t / t_0)^{\alpha}} + P_0 \quad (8)$$

where P denotes the percentage of nanoparticles staying in the original solution (i.e. the upper part of the tube) after t minutes' centrifugation; P_0 denotes the final percentage of nanoparticles left in the original solution after centrifugation for an infinite time; t_0 denotes the time in which half of the nanoparticles ((100–P_0)%/2) were transferred to the bottom solvent and α represents the sedimentation velocity. Increasing the centrifugation force led to an increase in the value of α but a decrease in P_0 and t_0, demonstrating the faster transpotation of nanoparticles from the original solvent to the new solvent through a water/oil interface. The mathmatical model and fitting curve were suitable for all the kinds of NPs mentioned above, proving its versatility.

In conclusion, we have shown that density gradient centrifugation through water/oil interfaces can purify and switch colloidal nanoparticles to a well-defined solvent at almost any concentration without aggregation. Such a one-step purification technique is independent of solvent and particle morphologies. Meanwhile, more than 99.9% of nanoparticles and only a small fraction (less than 10^{-4}) of the original impurities were transferred to the new solvent, demonstrating the high efficiency of the purification process. Furthermore, the switching process was also selective for nanoparticles with different sizes and morphologies. This purification and solvent switching method has been shown to be an efficient tool for post-treatment of colloidal nanoparticles synthesized in both aqueous and organic systems and thus should contribute to the mass production and applications of colloidal NPs.

Acknowledgements

This work was financially supported by the National Natural Science Foundation of China, the National Basic Research Program (No. 2011CBA00503), the Program for Changjiang Scholars and Innovative Research Team and the Fundamental Research Funds for the Central Universities.

Electronic Supplementary Material: Supplementary material (experimental details and supplementary figures) is available in the online version of this article at http://dx.doi.org/10.1007/s12274-014-0527-7.

References

[1] Yin, Y.; Alivisatos, A. P. Colloidal nanocrystal synthesis and the organic–inorganic interface. *Nature* **2005**, *437*, 664–670.

[2] Burda, C.; Chen, X.; Narayanan, R.; El-Sayed, M. A. Chemistry and properties of nanocrystals of different shapes. *Chem. Rev.* **2005**, *105*, 1025–1102.

[3] Xia, Y.; Xiong, Y.; Lim, B.; Skrabalak, S. E. Shape-Controlled synthesis of metal nanocrystals: Simple chemistry meets complex physics? *Angew. Chem. Int. Ed.* **2009**, *48*, 60–103.

[4] Wang, D.; Xin, H. L.; Hovden, R.; Wang, H.; Yu, Y.; Muller, D. A.; DiSalvo, F. J.; Abruña, H. D. Structurally ordered intermetallic platinum–cobalt core–shell nanoparticles with enhanced activity and stability as oxygen reduction electrocatalysts. *Nat. Mater.* **2013**, *12*, 81–87.

[5] Zhou, Z. Y.; Tian, N.; Li, J. T.; Broadwell, I.; Sun, S. G. Nanomaterials of high surface energy with exceptional properties in catalysis and energy storage. *Chem. Soc. Rev.* **2011**, *40*, 4167–4185.

[6] Wang, D. S.; Li, Y. D. Bimetallic nanocrystals: Liquid-phase synthesis and catalytic applications. *Adv. Mater.* **2011**, *23*, 1044–1060.

[7] Norris, D. J.; Efros, A. L.; Erwin, S. C. Doped nanocrystals. *Science* **2008**, *319*, 1776–1779.

[8] Huynh, W. U.; Dittmer, J. J.; Alivisatos, A. P. Hybrid nanorod–polymer solar cells. *Science* **2002**, *295*, 2425–2427.

[9] Liu, N.; Lu, Z.; Zhao, J.; McDowell, M. T.; Lee, H. W.; Zhao, W.; Cui, Y. A pomegranate-inspired nanoscale design for large-volume-change lithium battery anodes. *Nat. Nanotechnol.* **2014**, *9*, 187–192.

[10] Zrazhevskiy, P.; Gao, X. H. Quantum dot imaging platform for single-cell molecular profiling. *Nat. Commun.* **2013**, *4*, 1619.

[11] Xia, X.; Wang, Y.; Ruditskiy, A.; Xia, Y. 25th anniversary article: Galvanic replacement: A simple and versatile route to hollow nanostructures with tunable and well-controlled properties. *Adv. Mater.* **2013**, *25*, 6313–6333.

[12] Doane, T. L.; Burda, C. The unique role of nanoparticles in nanomedicine: Imaging, drug delivery and therapy. *Chem. Soc. Rev.* **2012**, *41*, 2885–2911.

[13] Ma, W.; Kuang, H.; Xu, L.; Ding, L.; Xu, C.; Wang, L.; Kotov, N. A. Attomolar DNA detection with chiral nanorod assemblies. *Nat. Commun.* **2013**, *4*, 2689.

[14] Strmcnik, D.; Uchimura, M.; Wang, C.; Subbaraman, R.; Danilovic, N.; van der Vliet, D.; Paulikas, A. P.; Stamenkovic, V. R.; Markovic, N. M. Improving the hydrogen oxidation reaction rate by promotion of hydroxyl adsorption. *Nat. Chem.* **2013**, *5*, 300–306.

[15] Wang, Y.; Chen, G.; Yang, M.; Silber, G.; Xing, S.; Tan, L. H.; Wang, F.; Feng, Y.; Liu, X.; Li, S. et al. A systems approach towards the stoichiometry-controlled hetero-assembly of nanoparticles. *Nat. Commun.* **2010**, *1*, 87.

[16] Wang, X.; Li, G.; Chen, T.; Yang, M.; Zhang, Z.; Wu, T.; Chen, H. Polymer-encapsulated gold-nanoparticle dimers: Facile preparation and catalytical application in guided growth of dimeric ZnO-nanowires. *Nano Lett.* **2008**, *8*, 2643–2647.

[17] Skrdla, P. J. Roles of nucleation, denucleation, coarsening, and aggregation kinetics in nanoparticle preparations and neurological disease. *Langmuir* **2012**, *28*, 4842–4857.

[18] Arnold, M. S.; Green, A. A.; Hulvat, J. F.; Stupp, S. I.; Hersam, M. C. Sorting carbon nanotubes by electronic structure using density differentiation. *Nat. Nanotechnol.* **2006**, *1*, 60–65.

[19] Mastronardi, M. L.; Henderson, E. J.; Puzzo, D. P.; Ozin, G. A. Small silicon, big opportunities: The development and future of colloidally-stable monodisperse silicon nanocrystals. *Adv. Mater.* **2012**, *24*, 5890–5898.

[20] Bai, L.; Ma, X.; Liu, J.; Sun, X.; Zhao, D.; Evans, D. G. Rapid separation and purification of nanoparticles in organic density gradients. *J. Am. Chem. Soc.* **2010**, *132*, 2333–2337.

[21] Li, S.; Chang, Z.; Liu, J.; Bai, L.; Luo, L.; Sun, X. Separation of gold nanorods using density gradient ultracentrifugation. *Nano Res.* **2011**, *4*, 723–728.

[22] Sun, X.; Tabakman, S. M.; Seo, W. S.; Zhang, L.; Zhang, G.; Sherlock, S.; Bai, L.; Dai, H. Separation of nanoparticles in a density gradient: FeCo@C and gold nanocrystals. *Angew. Chem. Int. Ed.* **2009**, *48*, 939–942.

[23] Chen, G.; Wang, Y.; Tan, L. H.; Yang, M.; Tan, L. S.; Chen, Y.; Chen, H. High-purity separation of gold nanoparticle dimers and trimers. *J. Am. Chem. Soc.* **2009**, *131*, 4218–4219.

[24] Xu, J.; Wang, H.; Liu, C.; Yang, Y.; Chen, T.; Wang, Y.; Wang, F.; Liu, X.; Xing, B.; Chen, H. Mechanical nanosprings: Induced coiling and uncoiling of ultrathin Au nanowires. *J. Am. Chem. Soc.* **2010**, *132*, 11920–11922.

[25] Brakke, M. K.; Daly, J. M. Density-gradient centrifugation: Non-ideal sedimentation and the interaction of major and minor components. *Science* **1965**, *148*, 387–389.